Evolution of pinch-and-swell structures in a power-law layer

Stefan M. Schmalholz [a,*], Daniel W. Schmid [b], Raymond C. Fletcher [b,c]

[a] *Department of Earth Sciences, Geological Institute, ETH Zurich, Leonhardstrasse 19, LEB D3, 8092 Zurich, Switzerland*
[b] *Physics of Geological Processes, University of Oslo, Oslo, Norway*
[c] *Department of Geosciences, Pennsylvania State University, University Park, PA 16803, USA*

Abstract

Analytical and finite element (FEM) solutions for the necking of a single power-law layer up to large finite amplitude are obtained. Continuous necking of the layer produces pinch-and-swell structures. The layer is either a free plate or embedded in a homogeneous medium. An analytical solution for finite amplitude necking based on the assumption that plane sections remain plane (PSRP) agrees well with the FEM result for a layer power-law stress exponent $n \leq 5$ and for a ratio of layer to medium effective viscosities $m \geq 100$. FEM simulations for embedded layers verify that PSRP for $m \geq 20$. The presented numerical experiments generate localized necking and pinch-and-swell structures similar to natural ones for $n \geq 5$ and $m > 20$. Additional weakening mechanisms, such as strain softening, although likely to be operative in nature, are not required to generate natural pinch-and-swell structures. FEM experiments with random perturbation of the layer interfaces show that even with strong necking instability the layer is thinned at the swell as well as at the necks, affecting strain estimation from pinch-and-swell geometry.
© 2008 Elsevier Ltd. All rights reserved.

1. Introduction

Pinch-and-swell structures (Fig. 1, see also Ramberg, 1955; Price and Cosgrove, 1990; Pollard and Fletcher, 2005) result from necking when a stiff layer and its weaker matrix are subject to layer-parallel extension, or, equivalently, layer-normal shortening (Kidan and Cosgrove, 1996). Pinch-and-swell structures form by continuous necking, while discrete boudins (Ramberg, 1955; Pollard and Fletcher, 2005) form by either mode I fracture or mode II faulting, often after some continuous necking.

Various natural structures on different scales are likely the result of necking. The regular alternation of basins and ranges in the Basin and Range Province, western United States (Fletcher and Hallet, 1983; Zuber and Parmentier, 1986), and that of analogous structures in the grooved terrain on the moon of Jupiter Ganymede (Dombard and McKinnon, 2001) can be interpreted as the result of selective amplification in necking. Necking in extension of the crust and lithosphere is a mechanism of sedimentary basin and continental margin formation (Bassi and Bonnin, 1988; Braun and Beaumont, 1989; Martinod and Davy, 1992). Regular spacing in small scale pinch-and-swell structures (Fig. 1D–F) clearly forms by necking and is the subject of the present paper.

Analysis of low-amplitude necking of an embedded layer yields the growth rate of a sinusoidal pure pinch-and-swell perturbation (Smith, 1977; Johnson and Fletcher, 1994) as a function of its wavelength to thickness ratio, L/T, and the rheological parameters m, n, and for the matrix, n_1 (see Table 1 for explanation of symbols). The most rapid amplification occurs at the dominant wavelength to layer thickness ratio, L_d/T (Fig. 2, Biot, 1961; Fletcher, 1974; Smith, 1977). These analytical results, valid for gentle interface slope with amplitude $A \ll L$, are not applicable to growth of pinch-and-swell structures with the large layer thickness variation that is commonly observed (Fig. 1). Few mathematical and experimental

* Corresponding author. Tel.: +41 44 632 8167; fax: +41 44 632 1030.
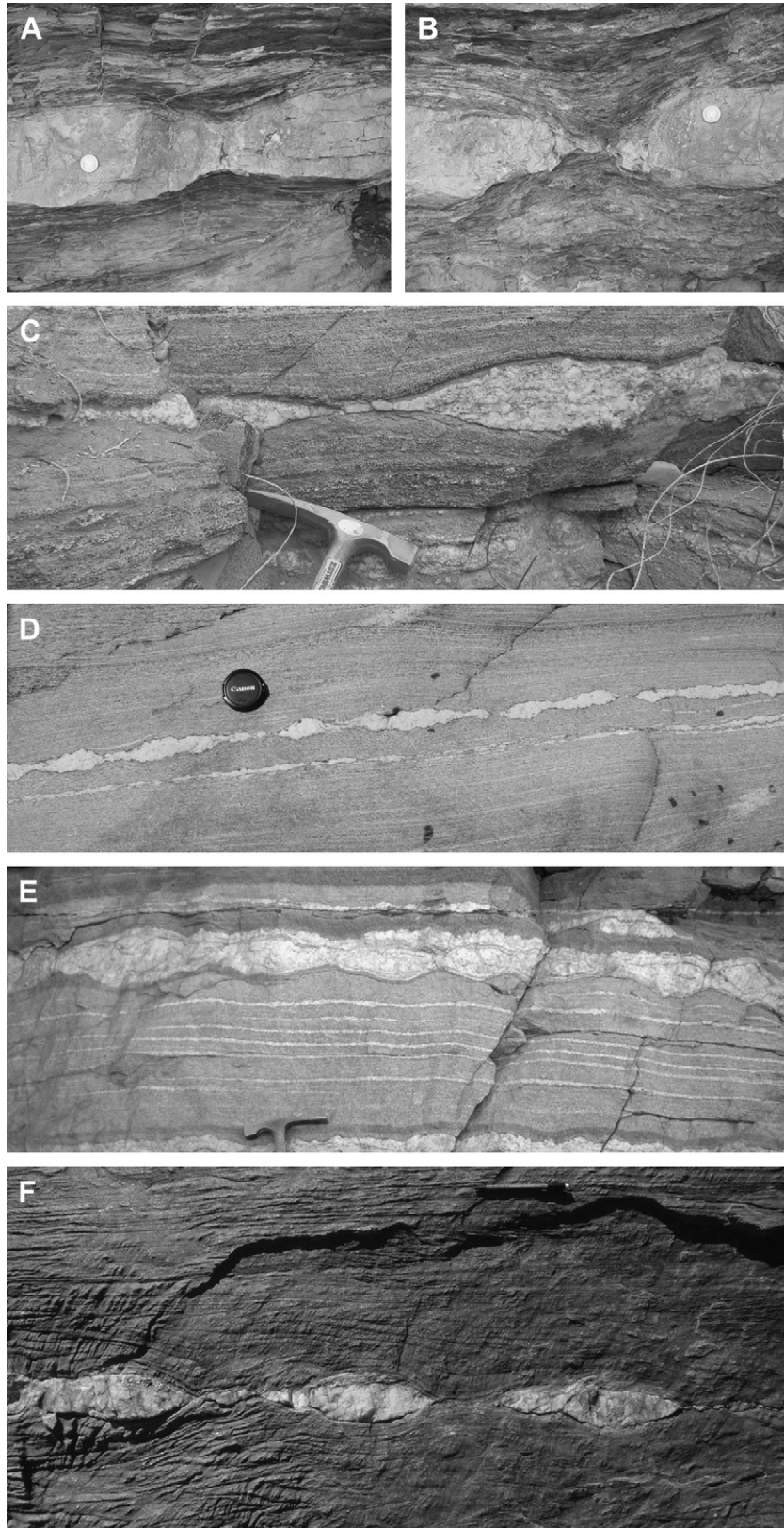 *E-mail address:* schmalholz@erdw.ethz.ch (S.M. Schmalholz).

Fig. 1. Natural examples of pinch-and-swell structures. (A) and (B) show limestone layers embedded in marls (Argovian) form the Ultrahelvetic Zone between the Morcles and Diablerets nappes, Swiss Alps, (C) shows metamorphic migmatites from Wadi Firan, Sinai, Egypt, (D) shows metamorphic migmatites from Valle Maggia, Swiss Alps (Photos A–D) by S.M. Schmalholz), (E) shows metamorphic migmatites from Canada (photo by J.-P. Burg, full picture can be seen on www. diogenes.ethz.ch), and (F) shows vein quartz in black calcite marble from Ugab region, Namibia (photo by N. Mancktelow).

Table 1
Explanation of symbols used in the text

Symbol	Explanation
A	Amplitude
A_0	Initial amplitude
T	Thickness of the layer
T_0	Initial thickness
L	Wavelength
L_0	Initial wavelength
L_d	Dominant wavelength
L_p	Preferred wavelength
k	Dimensionless wave number
k_d	Dominant wave number
$\overline{D}_{xx}$	Basic-state rate of extension
S	Stretch
q	Rate of amplification, growth rate
q_d	Dominant rate of amplification
n	Power-law exponent of the layer
n_1	Power-law exponent of the matrix
$\overline{\eta}$	Effective viscosity of the layer
$\overline{\eta}_1$	Effective viscosity of the matrix
m	Viscosity ratio: $\overline{\eta}/\overline{\eta}_1$
t	Time
B	Material constant
τ_{xx}	Layer-parallel deviatoric stress
F	Layer-parallel force

(Ramberg, 1955; Neurath and Smith, 1982; Mandal et al., 1992) studies have investigated the finite-amplitude evolution. An approximate analytical solution for fold growth to large amplitude (Schmalholz and Podladchikov, 2000) is not yet available for necking. Here, finite amplitude evolution of pinch-and-swell structures is studied with the numerical, finite-element method (FEM) to obtain results for nonlinear, large strain effects. An analytical solution for finite amplitude
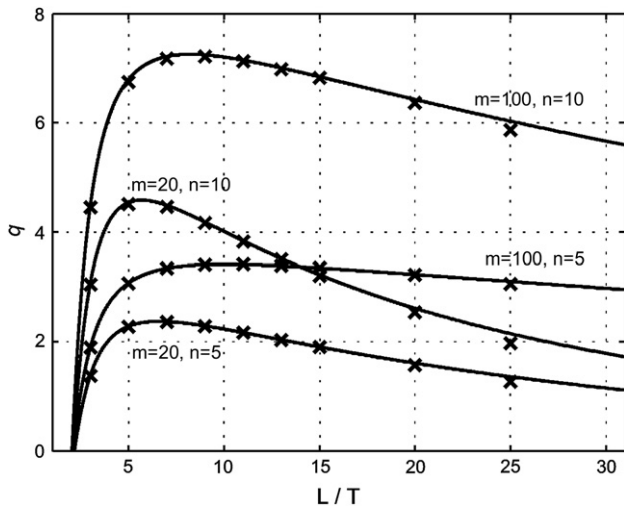

Fig. 2. The dispersion relation for power-law necking (eq. 2). The dimensionless growth rate of the layer perturbation, q, is plotted versus the ratio of wavelength to layer thickness, L/T. The dominant wavelength to layer thickness ratio, L_d/T, corresponds to the maximal value of q. The effective viscosity contrast, m, is 20 and 100, the power-law exponents of the layer, n, are 5 and 10 and the power-law exponent of the matrix is 1 (i.e. Newtonian matrix). The crosses have been numerically calculated with the FEM code (Appendix C) and agree well with the analytical solution.

necking of a free plate, based on the assumption that plane sections remain plane (PSRP), is also obtained. This is a modest modification of the treatment of Emerman and Turcotte (1984), following that of Hart (1967).

From the analytical treatment of selective amplification, a necking instability strong enough to generate the pinch-and-swell structure requires $n \gg 1$ (Smith, 1977; Emerman and Turcotte, 1984). This requirement is re-examined using the FEM solution. The evolution of pinch-and-swell structures from an initial random pinch-and-swell perturbation of the layer is compared with that obtained from the analytical development. Finally, we discuss the estimation of rheological properties and bulk strain from the geometry of natural pinch-and-swell structures.

2. Analytical solutions for necking

2.1. Thick-plate solution

The existence of regular arrays of pinch-and-swell structures implies selective amplification of linearly-independent wavelength components, suggesting a fully linearized treatment of the nonlinear constitutive relations and the boundary conditions (Fletcher, 1974). Only nonlinear materials develop a necking instability, and wavelength selection only occurs when the approximation of linear independence at small interface slope is valid.

For a pure sinusoidal pinch-and-swell perturbation with wavelength L and amplitude A (Fig. 3, the result for the fold mode is equation 8 in Fletcher, 1974):

$$\frac{1}{|\overline{D}_{xx}|A}\frac{dA}{dt} = q\,\mathrm{sgn}(\overline{D}_{xx}) \tag{1}$$

where $\overline{D}_{xx}$ is the basic state rate of extension and t is time. The thick-plate result for q is:

$$q = -1 + \frac{2n\left(1-\dfrac{1}{m}\right)}{(1-Q^2)+\dfrac{\sqrt{n-1}}{2\sin\beta k}\left[(1+Q^2)(e^{\alpha k}-e^{-\alpha k})+2Q(e^{\alpha k}+e^{-\alpha k})\right]} \tag{2}$$
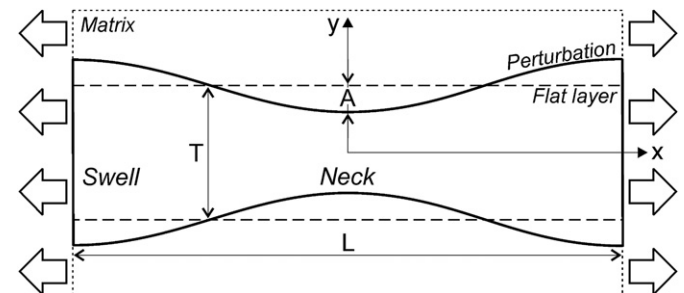

Fig. 3. Sketch of model setup for modelling necking and pinch-and-swell structures. A, T and L are the amplitude, thickness and wavelength of the layer exhibiting a power-law rheology, respectively. The imposed far field deformation is pure shear with extension parallel to the layer.

with

$$\alpha = \sqrt{\frac{1}{n}}, \quad \beta = \sqrt{1 - \frac{1}{n}}, \quad k = 2\pi\left(\frac{T}{L}\right), \quad m = \frac{\bar{\eta}}{\bar{\eta}_1},$$
$$Q = \sqrt{\frac{n}{n_1}\frac{\bar{\eta}_1}{\bar{\eta}}}.$$

q is plotted versus L/T in Fig. 2 using the Matlab script of Appendix A. In addition:

$$\frac{\mathrm{d}k}{\mathrm{d}t} = -2\overline{D}_{xx}k \tag{3}$$

Integration of eq. (1) in the approximation that k and other parameters are constant yields:

$$\frac{A}{A_0} \cong \exp(q\overline{D}_{xx}t) = S^q \tag{4}$$

where $S = \exp(\overline{D}_{xx}t)$ is the uniform basic-state stretch and A_0 is the initial amplitude. Evidently, the amplification, A/A_0, may be considered a function of S. Thus, amplification by factors of 2, 5, or 10 for 10% extension, or $S \approx 1.1$, requires $q \approx 7$, 17, or 24. q quantifies how much faster the amplification is relative to the uniform basic-state stretch; n and n_1 are the stress exponents of the layer and matrix; $\bar{\eta}$ and $\bar{\eta}_1$ are their effective viscosities at the rate of extension $\overline{D}_{xx}$. The first term in the right hand side of eq. (2) corresponds to the kinematic amplification, which plays a special role in necking by canceling the maximal value of the second term in the limit $n \to 1$.

For $k \ll 1$, or $L \gg T$, and $m \gg 1$, or $\bar{\eta} \gg \bar{\eta}_1$, eq. (2) may be approximated by:

$$q \cong \frac{n}{1 + \frac{k^2}{12} + \frac{n}{m\sqrt{n_1}k}} - 1 \tag{5}$$

with maximum:

$$q_d \cong \frac{n}{1 + \frac{k_d^2}{4}} - 1 \cong n - 1 \tag{6}$$

at the same L_d/T as in folding (Fletcher, 1974):

$$k_d = 2\pi\left(\frac{T}{L_d}\right) \cong \left(\frac{6n}{m\sqrt{n_1}}\right)^{\frac{1}{3}} \tag{7}$$

The subscript d refers to the "dominant value". The modest value of q_d in eq. (6) implies weak pinch-and-swell amplification in layers with stress exponents $n \sim 2$–10, typical of those obtained from creep experiments (e.g., Neurath and Smith, 1982).

The dependence of L_d/T and q_d on n and m, obtained from the thick-plate solution (2), is shown in Fig. 4. A value $q_d \geq 24$ requires $n > 30$ and $m > 20$.

An accurate computation of the maximum amplification, and the value L_p/T at which it occurs, is obtained by integrating eq. (1) with (2) and (3) to a specified stretch (Fig. 5). Thus,
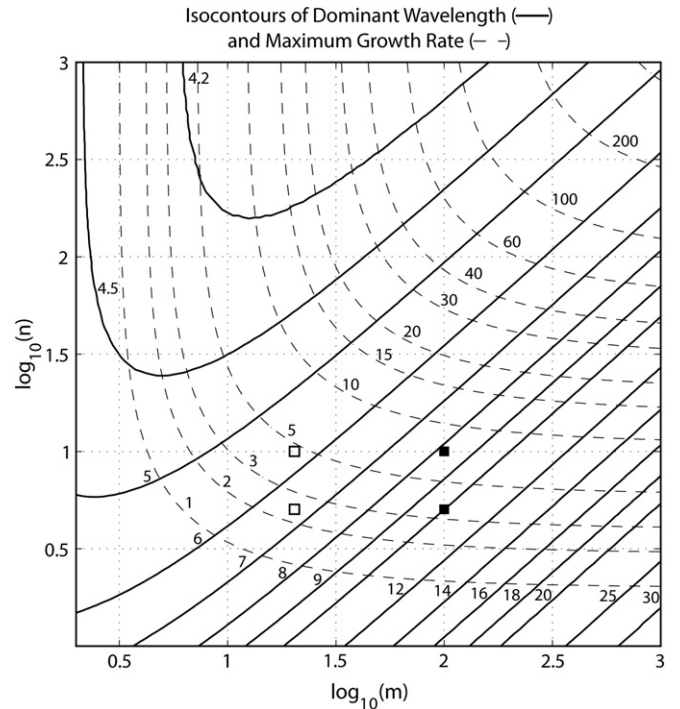

Fig. 4. Dominant wavelength to thickness ratio (L_d/T) and maximum relative rate of amplification (q_d) as a function of the rheological parameters n and m ($n_1 = 1$). The two open squares correspond to the parameters for numerical experiments shown in Fig. 13A ($n = 5$, $m = 20$) and E ($n = 10$, $m = 20$) and the filled squares correspond to the parameters for numerical experiments shown in Fig. 13B ($n = 5$, $m = 100$) and F ($n = 10$, $m = 100$). See text for further discussion.

the pinch-and-swell aspect ratio at termination of selective amplification, L_p/T, where L_p is the wavelength that has received the maximum amplification (subscript p refers to "preferred", see Sherwin and Chapple, 1968; Johnson and Fletcher, 1994), will be greater than L_d/T, opposite to the result in folding.

Note that after wavelength selection in pinch and swell breaks down at some value of the surface slope, extension concentrated at the neck continues, so that L_P/T cannot be readily estimated from field observations as it can for folds, which maintain approximately uniform thickness for a substantial interval of further shortening.

The large aspect ratio suggested by the above analysis tends not to be consistent with observations of the natural structures, such as those in Fig. 1. Strain softening (Neurath and Smith, 1982) would allow for a greater rate of necking with bulk extension. Alternatively, a geometric effect, operative without strain softening, might be associated with such pinch-off.

2.2. Plane sections remain plane (PSRP) solution for a free plate

The solution based on the approximation to 1st-order is not a valid solution for the evolution of the neck to large lateral variation in layer thickness. However, an analytical solution for the finite amplitude necking of a free plate may be
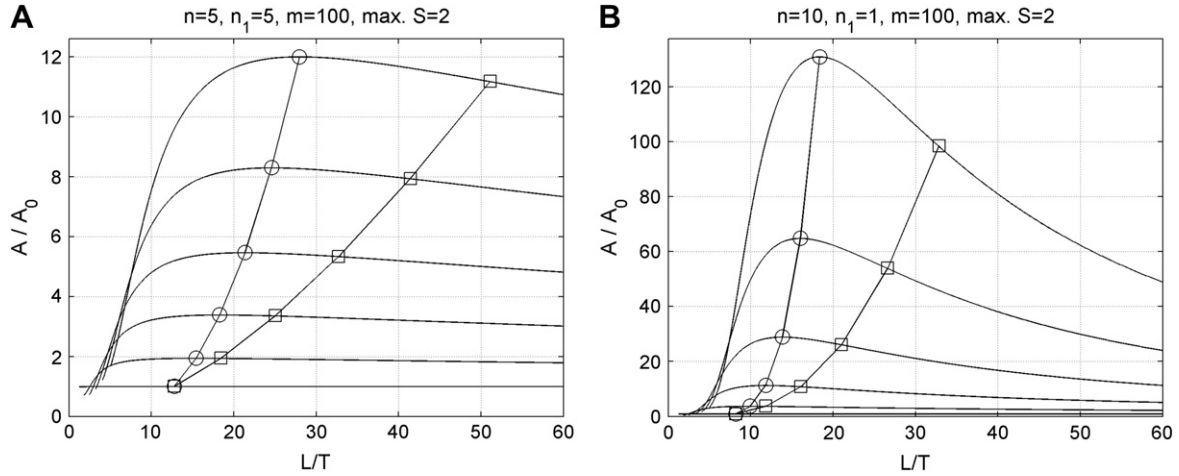
Fig. 5. Amplification (A/A_0) spectra for (A) $n = 5$, $n_1 = 5$, and $m = 100$; and (B) $n = 10$, $n_1 = 1$, and $m = 100$ for $S = 1$, 1.2,...,2. The circles connect paths of maximum amplification and the squares connect paths corresponding to the initial value of L_d/T which increases during extension. The value of L/T corresponding to the maximum amplification is termed L_p/T.

obtained based on the assumptions that vertical plane sections across the layer remain plane during deformation and that the layer surfaces are traction-free. Such a solution was given by Emerman and Turcotte (1984), who referred to a prior source in Hart (1967). We apply this solution to a layer extended at either constant force or constant rate of extension.

2.2.1. Constant force

By incompressibility in plane flow, the assumed uniform horizontal rate of extension, D_{xx}, of a vertical plane in the layer with local thickness T is:

$$D_{xx} = -\frac{1}{T}\frac{dT}{dt} \tag{8}$$

with d/dt being the total derivative with respect to time. For a free plate, the layer-parallel force, F, is uniform and the mean layer-parallel deviatoric stress is:

$$\tau_{xx} = \frac{1}{2}\frac{F}{T} \tag{9}$$

For a power-law fluid:

$$D_{xx} = B\tau_{xx}^n \tag{10}$$

where B is a material constant and n is the power-law exponent. Substituting eqs. (9) and (10) into (8) and solving for $T(t)$ with initial condition $T(0) = T_0$ yields:

$$T(t) = T_0\left[1 - nB\left(\frac{F}{2T_0}\right)^n t\right]^{\frac{1}{n}} \tag{11}$$

At a finite time, the minimum layer thickness goes to zero, since the rate of deformation at constant load tends to infinity as the layer thickness tends to zero. Requiring that a finite layer segment deforms at a mean constant rate of extension results, on the other hand, in a decreasing load as thickness tends to zero.

2.2.2. Constant rate of extension

Let a finite layer section be represented by an initial set of segments of equal width Δx^0 and variable thicknesses T_k^0, $k = 1,...,N$. We wish to extend the layer at a constant average rate of extension, using the PSRP approximation for a segment:

$$\frac{1}{\Delta x_k}\frac{d\Delta x_k}{dt} = -\frac{1}{T_k}\frac{dT_k}{dt} = B\left(\frac{F}{2T_k}\right)^n = B\left(\frac{F}{2}\right)^n\left(\frac{1}{T_k}\right)^n \tag{12}$$

Since the area of a segment is conserved:

$$T_k^0\Delta x^0 = T_k\Delta x_k \tag{13}$$

The mean rate of deformation is:

$$\overline{D}_{xx} = \frac{\sum_{k=1}^{N}\Delta x_k\left[B\left(\frac{F}{2T_k}\right)^n\right]}{\sum_{k=1}^{N}\Delta x_k} = \frac{B\left(\frac{F}{2}\right)^n\sum_{k=1}^{N}\left(\frac{T_k^0}{T_k^{n+1}}\right)}{\sum_{k=1}^{N}\left(\frac{T_k^0}{T_k}\right)} \tag{14}$$

Solving for the factor in (14) and substituting it into (12) yields:

$$\frac{dT_k}{dt} = -\left[\frac{\sum_{k=1}^{N}\left(\frac{T_k^0}{T_k}\right)}{\sum_{k=1}^{N}\left(\frac{T_k^0}{T_k^{n+1}}\right)}\right]\left(\frac{1}{T_k}\right)^{n-1}\overline{D}_{xx} \tag{15}$$

which may be integrated numerically. The profile is represented by a smooth curve connecting the mid-points of the horizontal elements of each segment. These have x-coordinates:

$$x_k = \frac{1}{2}(\Delta x_k - \Delta x_1) + \sum_{j=1}^{k-1}\Delta x_j$$

with origin at the mid-plane of the first segment. The Δx_k are obtained from eq. (13). Solutions for constant force and rate of extension can be plotted using the Matlab script provided in Appendix B. These two boundary conditions yield the same thickness evolution (Fig. 6). With respect to time the two differ, as constant force results in zero pinch thickness in a finite time and constant rate of extension does not. The stress and rate of deformation evolution inside the layer are different.

3. Finite element solution

Simulations of necking beyond the restrictions of the analytical treatment were obtained from specially developed two-dimensional finite element models (see Appendix C and Dabrowski et al., in press). The model set-up is shown in Fig. 3. A power-law layer is either embedded in matrix or treated as a free plate. Except for runs with random initial thickness variation, top and bottom interface were perturbed with a sinusoidal pinch-and-swell component at L_d/T. For the free plate, constant mean rate of extension is obtained by adjusting the horizontal velocities at the lateral boundaries at each time step. For an embedded layer, the uniform vertical velocities at the top and bottom of the matrix are adjusted to yield a uniform rate of far-field pure shear deformation. All initially planar boundaries are kept planar during deformation, and are treated as frictionless. The velocity field is calculated for the current geometry and boundary conditions and used to advance layer interfaces through a small time increment. The FEM solution has been successfully tested against the thick-plate analytical results for relative growth rate (Fig. 2). The boundary condition, uniform extension, based estimate (i.e. for $\varepsilon_{II} = 1$, see Appendix C) of the effective viscosity ratio between layer and matrix was either $m = 20$ or 100. This ratio only applies to the uniform extension of layer and medium. As structure develops, the effective viscosity becomes inhomogeneous (see Fig. 11 and Eq. (A4) in Appendix C).

4. Results

4.1. Pinch-and-swell evolution

Evolution of layer thickness at the neck and the swell depends on n and m (Fig. 6). The ratio $100(L - L_0)/L_0 = 100(S - 1)$, where L_0 and L are the initial and current widths of the layer, is used as the measure of bulk extension. The analytical PSRP solution yields identical results for either constant layer-parallel force or constant mean rate of extension. For $n = 5$ (Fig. 6A) the FEM solution for a free plate agrees well with the PSRP solution, but at $n = 10$ (Fig. 6B) the neck thickness decreases more slowly in the accurate FEM solution.

For the embedded layer, the thickness evolution depends strongly on m. Addition of a matrix retards thinning of the neck and enhances that of the swell, relative to those quantities
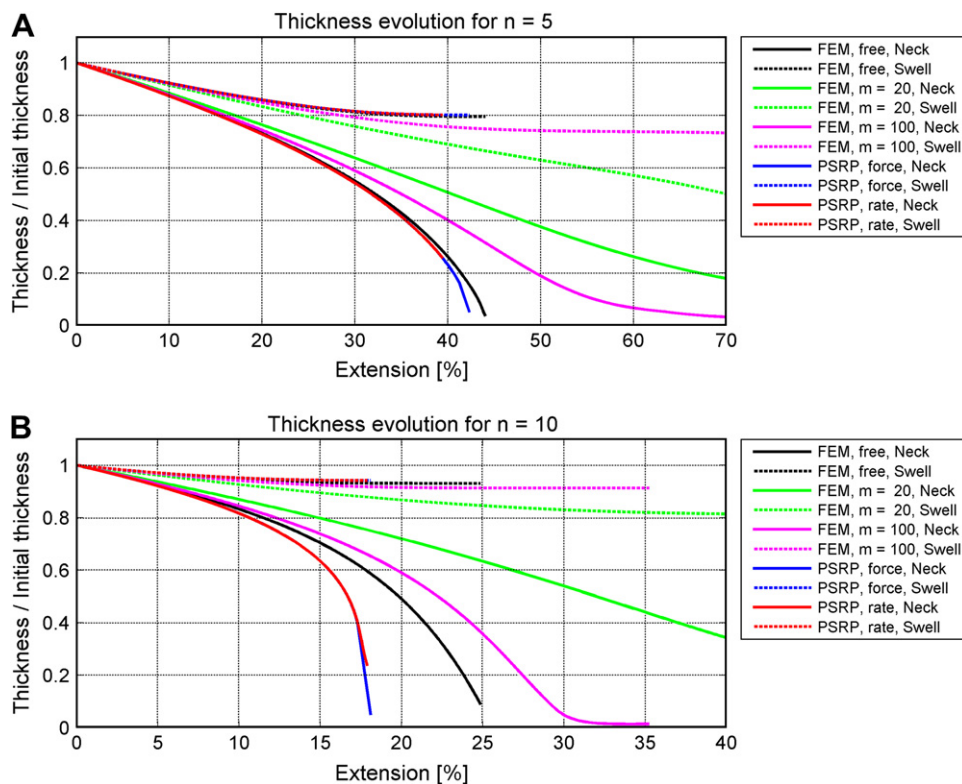

Fig. 6. Analytical PSRP and FEM solutions for layer thickness evolution with $n = 5$ (A) and $n = 10$ (B). FEM solutions are shown for a free plate and for an embedded layer. The PSRP solution is identical for constant extensional force and constant extensional strain rate. The FEM free plate solution is close to the PSRP solution for $n = 5$, but deviates significantly from the PSRP solution for $n = 10$.

for a free plate, as would be expected. Necking becomes less pronounced as m and n decrease.

For $n = 5$ the form of the pinch-and-swell obtained from the PSRP solution agrees well with the FEM result for a free plate (Fig. 7A and B). The assumption that PSRP is verified for an embedded layer with $m = 20$ and $m = 100$ ($n_1 = 1$, Fig. 7). Vertical lines in Fig. 7 are deformed multi-node grid lines, and in all cases studied, initially vertical grid lines really remain vertical and straight. At the neck, the layer surface for the free plate is cusp-like whereas, for embedded layers, it retains a nearly sinusoidal form.

If the Newtonian matrix is replaced by a power-law matrix with $n_1 = 5$, the thickness evolution at the neck is different (Fig. 8). In this simulation, L_0 was not adjusted to match the dominant wavelength for $n = 5$ and $n_1 = 5$, but kept at the value used for $n = 5$ and $n_1 = 1$. For $n_1 = 5$, the thickness evolution is much closer to that for the analytical free-plate PSRP solution, because the matrix nonlinearity allows strain rate softening as the deviatoric stress rises in the neck region.

4.2. Growth rate

The analytical solution gives, for the components with $L/T = L_d/T$ considered here, exponential growth in amplification, approximated as $A = A_0 \exp(q\overline{D}_{xx}t)$. A relative growth rate, $dA/dt/(A\overline{D}_{xx})$, equal to q in the low-slope case, may be determined from the numerical results by identifying the

difference between the swell and neck thicknesses as $2A$. The rate of change of $2A$ is calculated for each time step. The relative growth rate for the free plate is approximately constant with respect to extension for the case of $n = 5$, but increases slightly for $n = 10$ (Fig. 9). For embedded layers with $m = 100$, the relative growth rate decreases for $n = 5$, but is nearly constant for $n = 10$ up to an extension of about 25%, beyond which it decreases strongly (Fig. 9). For $m = 20$, the relative growth rate decreases continuously for both $n = 5$ and $n = 10$.

4.3. Evolution of the distributions of stress and effective viscosity

For the embedded layers (Fig. 10), the mean horizontal deviatoric stress across the layer first increases at the neck and then decreases after a certain amount of extension for values of $n = 5$ and $n = 10$. In contrast, at the swell this stress first decreases and then increases. For the free plate, the stress continuously increases at the neck but decreases at the swell. The stress changes are larger for $n = 10$ than for $n = 5$.

The local effective viscosity in an isotropic power-law fluid depends on the strain rate through the second invariant of the strain rate tensor, ε_{II} (eq. (A4) in Appendix C). For a homogeneous pure shear deformation without necking, $\varepsilon_{II} = 1$, given as a dimensionless quantity, and the behavior
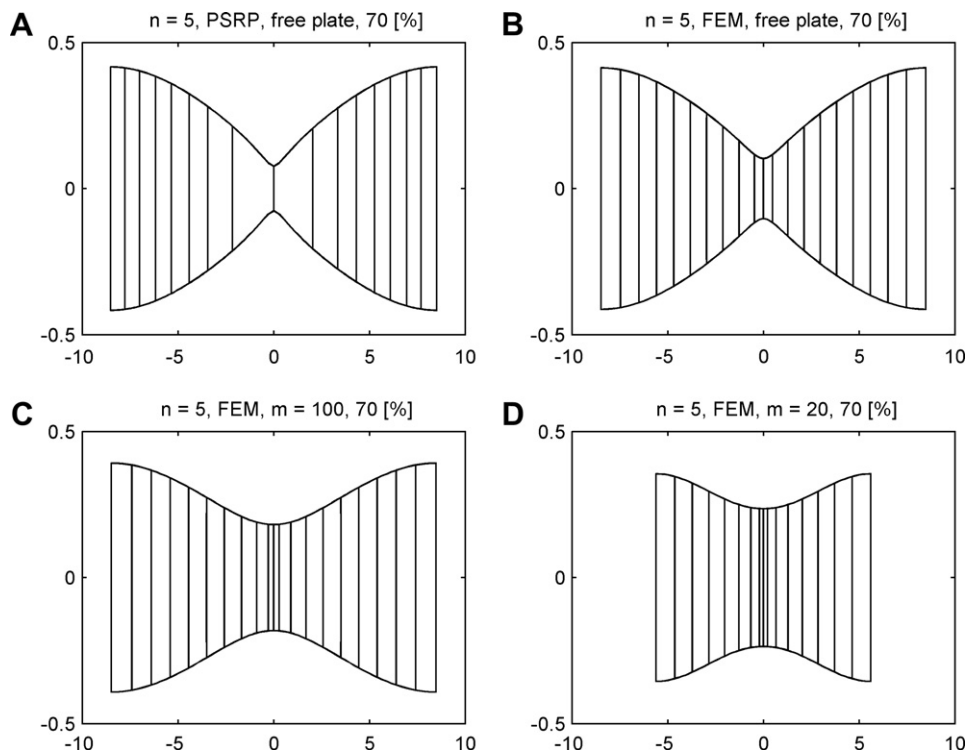

Fig. 7. Analytical and numerical results of neck geometries for an extensional strain of 70%. Note the vertical exaggeration: the individual box height is 1 and the width is 20. (A) corresponds to the PSRP solution, (B) corresponds to the FEM free plate solution, and (C) and (D) are numerical FEM results for embedded layers ($n_1 = 1$). The vertical lines are numerical multi-node grid lines which have been continuously deformed during the numerical simulation. The results demonstrate that the assumption that PSRP is valid also for embedded layers with small viscosity ratio (D).
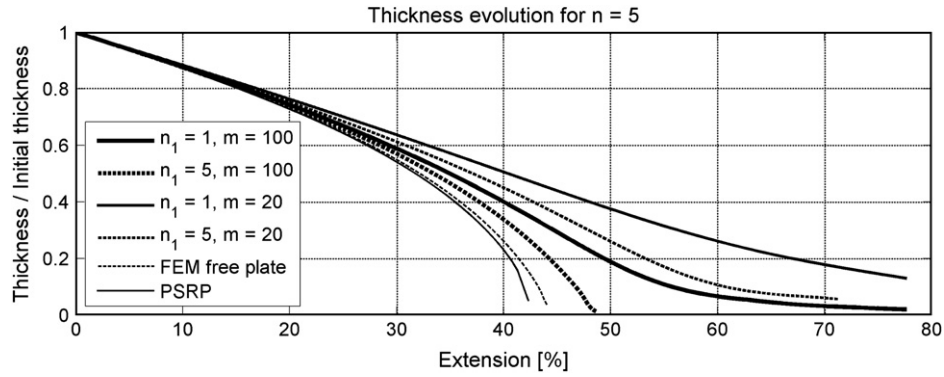
Fig. 8. Evolution of neck thickness for power-law layer and power-law matrix. The power-law exponent of the matrix material, n_1, has a considerable impact on the thickness evolution.

is effectively that of a Newtonian material. When the rate of deformation is inhomogeneous due to necking, ε_{II} is inhomogeneous. Where ε_{II} increases, the effective viscosity decreases and vice versa (Fig. 11). Thus, some areas in the model stiffen and others soften during the deformation. Necks soften markedly whereas swells stiffen. The strongest variation in effective viscosity can be observed for the model with $n = 10$ and $n_1 = 10$. In this model, two bands of lower effective viscosity occur within the matrix. These bands form an angle of about 90°, which would correspond to the angle of incipient shear bands in a plastic material with a von

Mises yield criterion at yield, corresponding to the limit $n_1 \rightarrow \infty$. Note that values of $n = 10$ and $n_1 = 10$ cause a strong necking instability for a viscosity ratio of 20 (Fig. 11D).

4.4. Evolution of sinusoidal and random pinch-and-swell

To study salient features in the evolution of simple structures, the initial perturbation was taken as a sinusoidal, symmetric pinch-and-swell. The forms of the resulting pinch-and-swell structures show a marked variation with n and m (Fig. 12). For
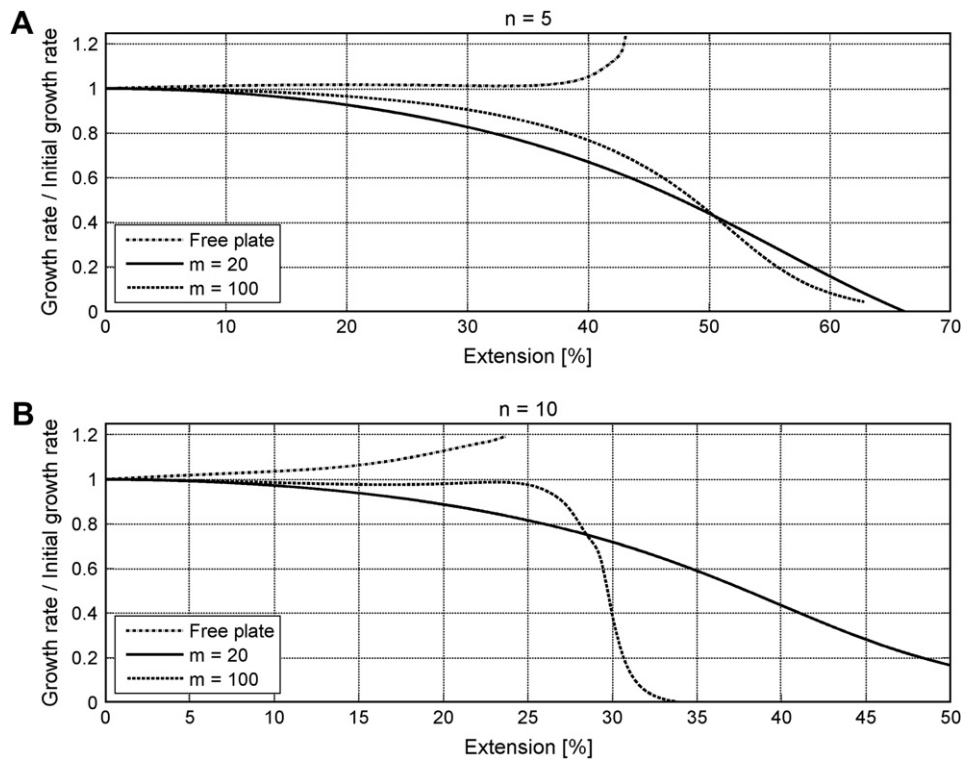

Fig. 9. Evolution of the relative growth rate of the layer perturbation for different values of n ($n_1 = 1$). The growth rates for the FEM free plate models are slightly increasing while the growth rates for the embedded models are decreasing. The growth rates for viscosity ratios $m = 100$ first decrease slower, but after a certain amount of extension faster than for values of $m = 20$. Note that for $n = 10$ and $m = 100$ the growth rate is more or less constant up to an extension of about 25% but then decreases strongly.
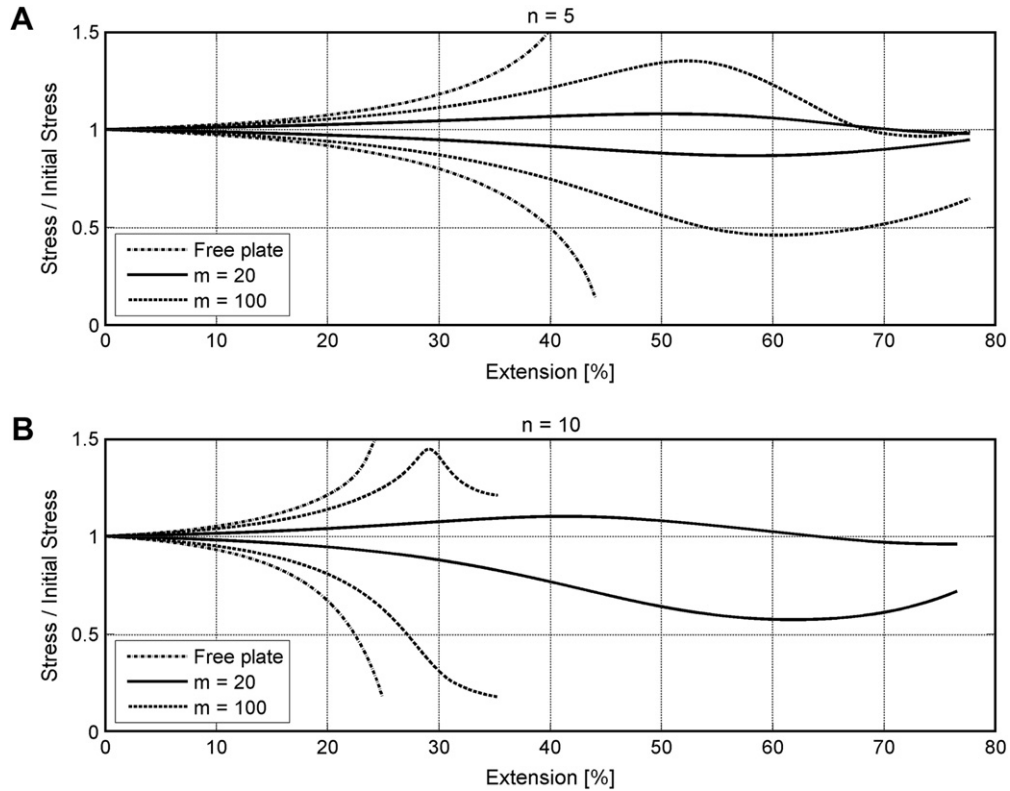
Fig. 10. Evolution of horizontal deviatoric stress, averaged across the layer, at the neck and swell. The lines above 1 correspond to stress values at the neck (or pinch) and the lines below 1 correspond to stress values at the swell. The larger the effective viscosity ratio, the larger the difference in stress at the neck and swell.

small values of n and m the layer is also thinned considerably at the swell and structures equivalent to natural pinch-and-swell structures do not develop. Such pinch-and-swell structure does develop provided $n \geq 5$ and $m > 20$.

In nature, the initial perturbation is generally random. A plausible assumption is that the natural perturbation will have the properties of "red noise", with amplitude proportional to wavelength. Numerical experiments were run with

interfaces perturbed by red noise (Fig. 13). The two surfaces are given independent initial perturbation, each with a maximum difference in vertical coordinate along the layer equal to 1/20th the initial layer thickness. For comparison, the same perturbation was used for each experiment on layers of unit initial thickness and length of 70 units. The exception is an experiment (Fig. 13H) where the perturbation of one surface is the mirror image of the other.
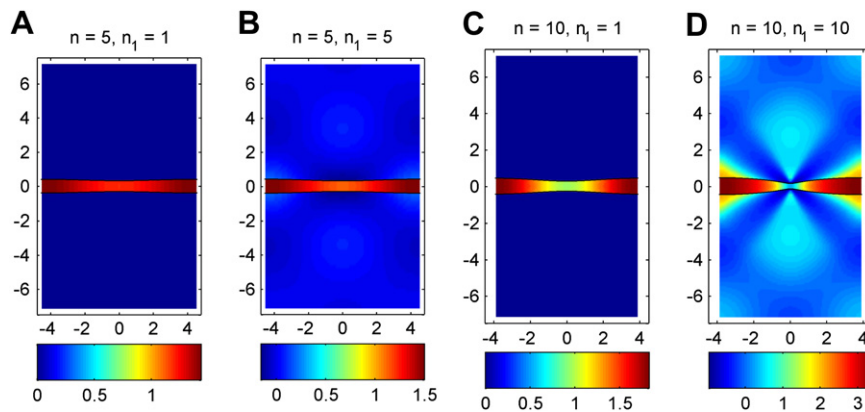
Fig. 11. Distribution of the effective viscosity (η_{eff}, see eq. (A4) in Appendix C) for different values of the power-law exponent in the layer, n, and the matrix, n_1. All graphs correspond to an extension of 39% and an effective viscosity ratio of 20. The values of the colorbar are the log10 of the effective viscosity. Red corresponds to high effective viscosities and blue to low effective viscosities. The effective viscosity varies by up to 4 orders of magnitude, and a strong variation is observable within the layer especially in (D).

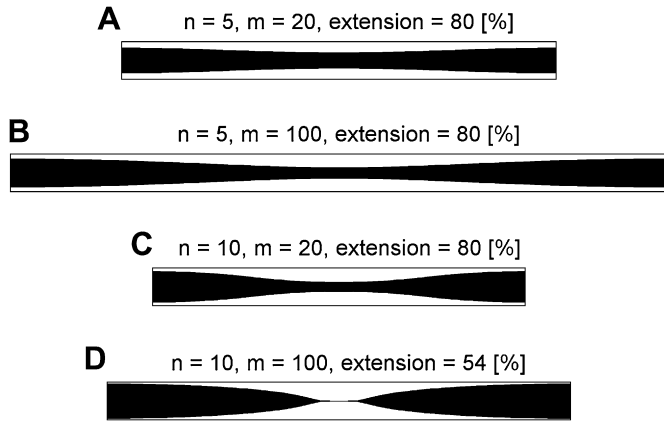Fig. 12. Large strain geometries of numerically modeled pinch-and-swell structures for Newtonian matrix. No vertical exaggeration. Boxes around layers show initial layer thickness to emphasize overall layer thinning. The initial sinusoidal perturbations corresponded to the dominant wavelength, L_d/T, yielding different initial length to thickness ratios of the four layers. Varying the power-law exponent from 5 to 10 and the effective viscosity ratio from 20 to 100 has a major impact on the pinch-and-swell geometries.

As expected, the strongest instability occurs for the largest values, $n = 10$ and $m = 100$. The relative strength of necking instability for the random perturbation is the same as for the initial sinusoidal forms. The height of the box around each layer in Fig. 13 equals the initial layer thickness. Layers with weak necking instability (Fig. 13A,B,C,E) show significant thinning over their entire length, but strongly necked layers (Fig. 13D,F,G) also show significant thinning at swells. In strain estimation by interpretation of pinch-and-swell geometries, the ratio of swell thickness to neck thickness is usually used to estimate strain, assuming the swells preserve initial thickness (e.g., Pollard and Fletcher, 2005). Such a method therefore gives a lower bound for strain.

5. Discussion

Every mathematical model is always a simplification of a natural process that aims to describe its essential features with a minimal number of assumptions. Such an aim is expressed in the well known principle of logic termed the *lex parsimoniae* or Ockham's razor (e.g. Kneale and Kneale, 1985). We have shown here that pinch-and-swell may be generated in a power-law layer with $n \geq 5$, but not in a Newtonian viscous layer $n = 1$ (see also Fletcher, 1974; Emerman and Turcotte, 1984). Such nonlinear power-law behavior is observed in steady-state creep experiments (e.g. Carter and Tsenn, 1987) and the values for n and m used in this study are within the range of experimental values. For dislocation creep, typical values of n lie between 3 and 5, but values as large as 8 are obtained. Therefore, the constant-property power-law fluid is the simplest experimentally established behavior that yields pinch-and-swell structure. Additionally, experimental values obtained on the centimeter scale for homogeneous rock samples and laboratory deformation rates may be smaller than the effective values for natural,

heterogeneous rocks and geological deformation rates on the meter scale. In nature, many deformation mechanisms act simultaneously at different scales, but at the scale of observation, they may be represented by power-law creep. A more complex model for pinch-and-swell formation would be justified if it were required to fit other observations, such as microstructural observations, in addition to the pinch-and-swell geometry.

Applying damage mechanics, Turcotte and Glasscoe (2004) and Nanjo et al. (2005) showed that the brittle deformation can be modeled by power-law constitutive relations, with stress exponent between 5 and 15. Neurath and Smith (1982) show that strain softening in a power-law fluid increases the effective power-law exponent in necking, and this may exceed 15. We show that $n = 5-10$ in both layer and matrix and $m > 20$ suffice to generate significant necking instability, producing structures similar to natural pinch-and-swell structures. Thus, while they may be operative, weakening mechanisms such as strain softening or shear heating need not be evoked.

To obtain estimates of rheological parameters such as n and m from measurements of natural pinch-and-swell structure, it is tempting to follow the method that Sherwin and Chapple (1968) applied to data from natural single-layer folds (see also Fletcher, 1974; Fletcher and Sherwin, 1978; Hudleston and Holst, 1984). Such a method might be tested using the simulations of pinch-and-swell structures derived from the random initial perturbation of a long layer segment. As a first step, we compute the amplification spectrum for a specified set of values n, n_1, and m taking into account the basic-state layer-parallel extension. Results for the parameters used in the two simulations that showed the strongest structural development after 80% extension ($S = 1.8$) are shown in Fig. 13F and H. Fig. 5A shows the amplification spectra at stretches $S = 1$, 1.2, 1.4,…,2 for $n = 5$, $n_1 = 5$, and $m = 100$; Fig. 5B shows the result for $n = 10$, $n_1 = 1$, and $m = 100$. In these figures, the steeper curve connects maxima in amplification. The value of the "preferred" wavelength to thickness ratio, L_p/T, increases, but the rate of increase decreases with stretch, and the final ratio is much less than that of the component initially at the maximum of the spectrum, shown by the gentler curve. After an amplification of 10, $L_p/T \approx 2\ L_d/T$ (Fig. 5A) and $L_P/T \approx 1.5\ L_d/T$ (Fig. 5B). This selective amplification approximates that achieved in the random perturbation experiments. At $n = 5$, $n_1 = 5$, and $m = 100$, the maximum amplification is only 8 at $S = 1.6$, and there is little selectivity, except against small L/T. For $n = 10$, $n_1 = 1$, and $m = 100$ (Fig. 5B), maximum amplification and selectivity are both significantly greater, although the latter is still modest.

Low selectivity of the larger layer segments may be tied to the development of extremely attenuated necks (Fig. 13F and H). The resulting segmentation of the layers slows down the growth of instability in the segments. Once a single pinch is developed, such as in Fig. 13D, the layer is no longer subject to the full rate of extension applied at the lateral boundaries. Extension in the neck-bounded layer segments is then driven only by shearing of the matrix along its surfaces. Schmid et al. (2004) investigated the corresponding situation of
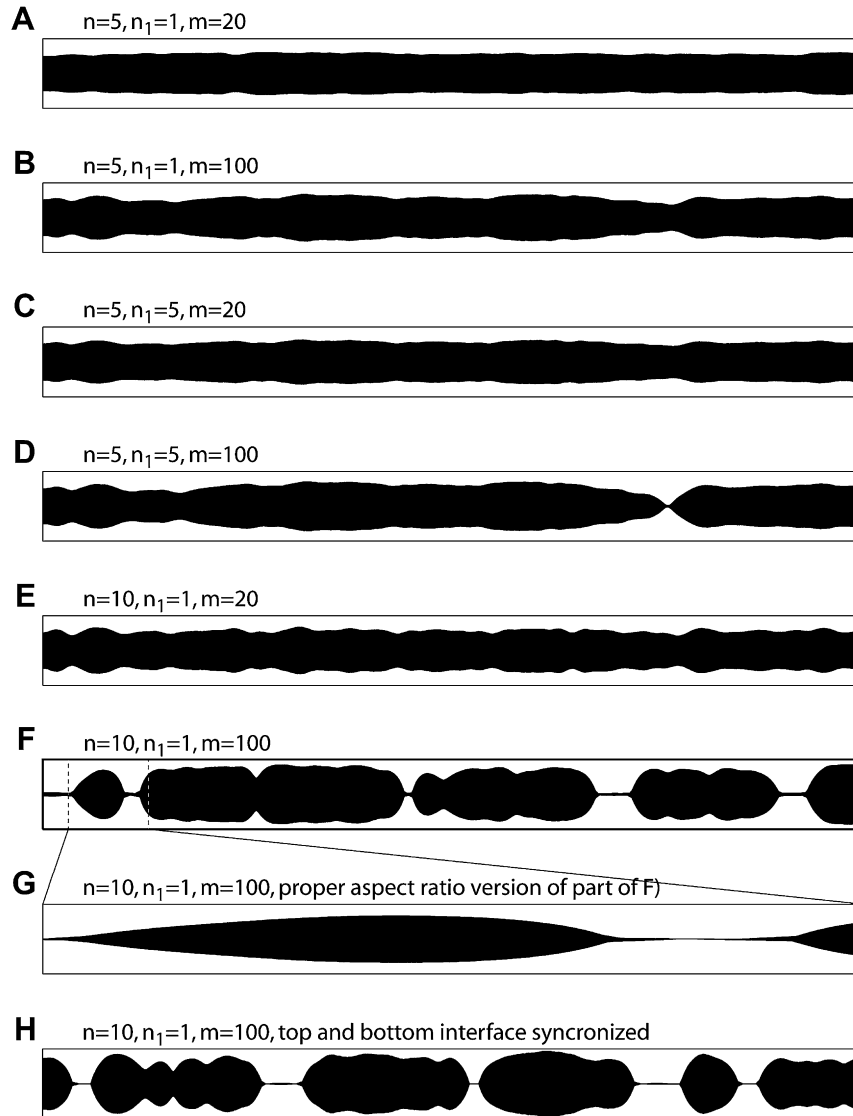
A   n=5, n₁=1, m=20

B   n=5, n₁=1, m=100

C   n=5, n₁=5, m=20

D   n=5, n₁=5, m=100

E   n=10, n₁=1, m=20

F   n=10, n₁=1, m=100

G   n=10, n₁=1, m=100, proper aspect ratio version of part of F)

H   n=10, n₁=1, m=100, top and bottom interface syncronized

Fig. 13. Pinch-and-swell geometries after 80% extension for randomly perturbed layer interfaces. Note the vertical exaggeration: the individual box height is 1 and the length 126. The exception is (G) which shows part of (F) with the correct aspect ratio. It is evident that systems where only the layer exhibits a power-law rheology with $n = 5$ (A and B) do not show a significant necking instability. If both layer and matrix are in the power-law regime with $n = 5$ and $n_1 = 5$ (C and D) then an effective viscosity contrast of 100 is sufficient to develop a necking instability that is substantially faster than the passive layer thinning. Simulations with $n = 10$ and $m = 100$ develop the strongest necking instability (F and H). Reduction of the effective viscosity contrast to 20 significantly weakens the necking instability (E). The effect of an a priori interface synchronization (mirroring along the mid-plane) that is assumed by the thick plate solution does not change the results drastically, compare (F) and (H).

folding. They found that if the effective aspect ratio of width to thickness, a/b, of a layer segment is less than the effective viscosity ratio, m, the rate of shortening in it decreases significantly relative to the far-field value and growth of folds is slowed. The same applies in the inception of pinch-and-swell in extension. The small connectors between boudins can be ignored, and the rate of extension inside the layer segment is:

$$D_{xx}^l \approx \frac{1}{1 + \frac{2mb}{a}} D_{xx}^0 \qquad (16)$$

where D_{xx}^0 is the far-field value. Note the large vertical exaggeration in Fig. 13, illustrated in sections F and G. Segmentation leads to preservation of weakly developed necks within segments (Fig. 13F and H). The effect of reducing the rate of extension inside the layer is amplified due to the nonlinear power-law rheology, which causes large effective viscosities in the isolated segments (for example swell regions in Fig. 11D). This causes a rapid decrease in the further development of the incipient pinches that can be observed in the isolated segments in Fig. 13F. Furthermore, the increase of effective segment viscosities is associated with an increase in L_d/T that also inhibits the growth of previously initiated pinches. Therefore, the layer

segmentation must be considered a key controlling factor in the finite strain development of pinch-and-swell structures.

Are the structures produced in the numerical models like those observed in the field? The extensive data sets required in the method of Sherwin and Chapple (1968) and others are not yet available, and we draw only a few preliminary conclusions here. Pinch-and-swell structures of Fig. 1E have aspect ratios of 4.7, 3.3, 3.3, and 3.5, and of Fig. 1F of 3.8 and 5.3, with only two larger than the minimum of the present model, $L_d/T = 4$ in the limit $n \rightarrow \infty$ (Fig. 4). These structures thus could not have formed by the necking of a homogeneous, constant-property power-law layer. Such small aspect ratio structures have been produced in a stiff layer embedded centrally in a soft layer of finite thickness bounded by much stiffer media (unpublished). Selectivity is markedly increased relative to the single-layer case, but strong instability requires much larger values of n—e.g., $n = 100$. The suggestion that the layer in Fig. 1E is embedded in a softer layer of finite thickness is tenable. The shapes and pinch-and-swell aspect ratios in Fig. 1C and D are comparable to those obtained in the present simulations (compare Figs. 12D, 13F and G). The single, localized neck in the limestone layer shown in Fig. 1B is similar to localized necking in the simulation shown in Fig. 13D. Our results indicate that $n = 5-10$ and $m = 20-100$ are lower limits for embedded constant-property power-law fluid layers showing pinch-and-swell structure.

For $n \leq 5$, the PSRP and free plate FEM solutions give closely similar swell and neck thicknesses to large extension. For $n > 5$, the PSRP and FEM solutions agree for swell thickness, but the PSRP solution shows more rapid reduction in neck thickness. Due to the strong material non-linearity, the neck becomes sharper and deformation no longer depends only on the mean horizontal stress as in the PSRP approximation. The same effect is observed for small aspect ratio perturbations of the free plate, since the approximation is only valid when the thickness gradient along the layer is small. No dependence on initial amplitude was observed on the agreement of PSRP and FEM, within the range of perturbation amplitudes between 1/100th and 1/10th of the layer thickness.

At finite amplitude, the growth rate of the necking instability, as now measured by the rate of change of the ratio of the thickness of a neck to that of the adjacent swell(s), decreases with increasing extension. However, for the larger values of m the growth rates first decrease slower than for smaller values of m but then decrease faster after a certain amount of extension (Fig. 9). This is different from the evolution of the growth rate for folding, where the higher growth rates for larger viscosity contrasts decrease faster than the growth rates for smaller viscosity contrasts (Schmalholz, 2006). For $n = 10$ and $m = 100$ the growth rate actually stays constant for about 25% of extension. The behavior that higher growth rates decrease slower with progressive extension indicates that an increase in either n or m results in a considerable stronger necking instability where much less extension will be required to achieve a certain thinning. The characteristic differences in the growth rate evolution for different values of n and m are

caused by nonlinear, large strain effects and cannot be predicted with analytical methods, so a numerical method is essential.

The evolution of the neck thickness with progressive extension shows two types of behavior (Fig. 6). For the free plate and embedded power-law layers with large n and m, thickness versus extension curves are strongly convex upwards. For small n and m, thickness versus extension curves show a concave upwards shape after some extension. Layers exhibiting strong convex upwards thickening curves are likely to be segmented after sufficient extension, whereas layers exhibiting concave upwards thickening curves are likely to develop wide-necked pinch-and-swell structures (Mandal et al., 1992).

Simulations displayed in Figs. 12 and 13 show two types of pinch-and-swell structures that are similar to those in the stable and unstable regime according to Mandal et al. (1992). Mandal et al. (1992) base discrimination of two neck types on experimental observation of lateral neck propagation with disappearance of swells after sufficient extension. Such observations are not seen in our numerical simulations. Mandal et al. (1992) performed experiments without an embedding medium, and used rods instead of plates, both significant differences from the present numerical models. Perhaps more significantly, the material used by Mandal et al. (1992) is not a power-law fluid, but viscoelastic and strain hardening. Embedded power-law layers did not exhibit the behavior they observed.

The numerical simulations verify the assumption that PSRP during necking. This result may be important for kinematic modeling of lithospheric necking, in which lithosphere is subdivided into a number of aligned columns that are thinned using different thinning factors (e.g. Kooi et al., 1992). Each column is assumed to thin and extend by pure shear alone, as in the PSRP approximation. Kinematic thinning models require significantly less computation than fully dynamic models, and therefore may be used efficiently to restore the thermo-tectono-stratigraphic evolution of a sedimentary basin (e.g. Poplavskii et al., 2001; Rüpke et al., in press).

6. Conclusions

The analytical PSRP solution for a free plate agrees well with the FEM solutions for power-law stress exponent $n \leq 5$ and viscosity ratios $m \geq 100$. The low-amplitude dispersion curve and the PSRP solution constitute a powerful analytical framework for investigating the formation of pinch-and-swell structures in power-law layers. Also, the dispersion curve for relative growth rate is an important tool to test numerical models with non-linear power-law rheologies, such as the FEM algorithm applied in this study, in order to guarantee correct numerical results.

Dependence of the necking behavior on power-law stress exponents and viscosity ratios is strong. Values of $m = 100$ and $n = 5-10$ are sufficient to produce pinch-and-swell forms similar to those observed in nature. Power-law stress exponents of the matrix $n_1 \geq 5$ significantly increase the necking

instability, and generation of pinch-and-swell forms similar to those observed in nature takes place for values of m smaller than the ones required for $n_1 = 1$. Additional weakening mechanisms, such as strain softening, although likely to be operative, are not required to generate natural pinch-and-swell structures.

The finite amplitude evolution of pinch-and-swell structures and buckle-folds is considerably different, although for both, the low-amplitude dispersion curves yield the same dominant wavelength. A pinch-and-swell component extends throughout its formation, so that waveform selection is a continuous process, while in folding, a waveform, at L_p/T, is selected (locked) and buckles without further significant change in arc-length and layer thickness.

The swell of a pinch-and-swell structure may also thin significantly during necking and estimates of bulk strain based on the relative thickness of neck and swell have to be carried out with care.

Acknowledgments

Appendix A. Matlab script for plotting the analytical dispersion relation for necking (thick plate, see eq. 2)

```
% Dispersion relation for necking
% Ray Fletcher
clear variables, close all, clc;
L_T       = 0.01:0.01:40;          % Wavelength to thickness array
n         = 10;                    % power-law exponent layer
n1        = 1.001;                 % Power-law exponent matrix
R         = 1/20;                  % Viscosity contrast between matrix and layer
phi       = 1;
a         = sqrt(1/n);
beta      = sqrt(1-1/n);
k         = 2*pi*(1./L_T);
Q         = sqrt(n/n1)*R;
q         = -1+(2*n*(1-R))./...
  ((1-Q^2)+phi*(sqrt(n-1))./(2*sin(beta.*k)).*...
  ((1+Q^2).*(exp(a*k)-exp(-a*k))+2*Q*(exp(a*k)+exp(-a*k))));
[qmax,imax] = max(q);
L_T_max    = L_T(imax);

plot(L_T,q,'-k','linewidth',1.5)
hold on
plot([L_T_max L_T_max],[min(q) qmax],'--k')
plot([min(L_T) L_T_max],[qmax qmax],'--k')
xlabel('L / T')
ylabel('q ')
title(['Dispersion relation for necking. n = ',num2str(n),', n_1 = ',num2str(n1,2)])
```

Appendix B. Matlab script for the analytical PSRP solution

```
% Matlab script for pinch-and-swell evolution in power-law fluids
% Ray Fletcher, Stefan Schmalholz & Dani Schmid
clear variables, close all, clc;
% INPUT PARAMETERS ======================================
n          = 5;            % Power-law exponent
amplitude  = 0.04;         % Initial amplitude of perturbation
width      = 10;           % Initial width
B          = 1;            % B-coefficient
F          = 1;            % Constant force
nx         = 201;          % Number of horizontal columns
% SET-UP OF GEOMETRY AND TIME ==========================
X_vec      = linspace(0, width, nx);
H_vec      = 1+amplitude*cos(X_vec/width*2*pi);  % Thickness
h0         = min(H_vec);
nt         = 1000;
t_tot      = (-2^n*(-(F/h0)^(-n) + (0.02*h0/F)^n)/n/B);
T_vec      = linspace(0, t_tot, nt);             % Time
dt         = T_vec(2)-T_vec(1);
[X, TIME]  = meshgrid(X_vec, T_vec);
[H, TIME]  = meshgrid(H_vec, T_vec);
Exx_bulk(1)= NaN;
X_vec_cs   = linspace(0, width, nx);
H_vec_cs   = 1+amplitude*cos(X_vec_cs/width*2*pi);
[Xcs, TIME_cs] = meshgrid(X_vec_cs, T_vec);
[Hcs, TIME_cs] = meshgrid(H_vec_cs, T_vec);
% TIME LOOP ============================================
for tstep=2:nt
  % Solution for constant force
  H(tstep,:)  = F.*(-2^n./(dt*n*B - 2^n*(F./H(tstep-1,:)).^(-n))).^(-1/n);
  Exx         = -(H(tstep,:)-H(tstep-1,:))./H(tstep-1,:)/dt;
  Dx          = diff(X(tstep-1,:));
  Dx_new      = Dx + dt*Dx.*((Exx(2:end)+Exx(1:end-1))./2);
  X(tstep,:)  = cumsum([0,Dx_new]);
  Exx_bulk(tstep) = (X(tstep,end)-X(tstep-1,end))/X(tstep-1,end)/dt;
  % Solution for constant strain rate
  S1          = sum(Hcs(tstep-1,:)./Hcs(tstep,:).^(n+1));
  S2          = sum(Hcs(tstep-1,:)./Hcs(tstep,:));
  Dx_mean     = B*(F/2)^n*S1/S2;
  Hcs(tstep+1,:) = Hcs(tstep,:) - dt.*(S2./S1).*(1./Hcs(tstep,:)).^(n-1)*Dx_mean;
  Dxcs        = diff(Xcs(tstep-1,:));
  Dxcs_new    = Hcs(tstep,1:end-1).*Dxcs./Hcs(tstep+1,1:end-1);
  Xcs(tstep,:) = cumsum([0,Dxcs_new]);
end
% PLOTTING RESULTS ======================================
figure1     = figure('units','normalized','position',[0.0992188 0.506836 0.4375 0.410156]);
step        = 0;
for tstep=[1 round(nt*0.97) nt-1];
  step      = step+1;
  subplot(310+step)
  plot(X(tstep,:)-X(tstep,end)/2, H(tstep,:), '-k', X(tstep,:)-X(tstep,end)/2, -H(tstep,:), '-k')
  hold on
  plot([X(tstep,1)-X(tstep,end)/2 X(tstep,1)-X(tstep,end)/2],[-H(tstep,1) H(tstep,1)],'-k')
  plot([X(tstep,end)-X(tstep,end)/2 X(tstep,end)-X(tstep,end)/2],[-H(tstep,end) H(tstep,end)],'-k')
  axis equal;
  axis([-max(X(end,:)/2)*1.1 max(X(end,:)/2)*1.1 -1.5-amplitude*2 1.5+amplitude*2]); drawnow
  Extension  = ((X(tstep,end)-X(tstep,1))-width)/width*100;
  title(['Extension = ',num2str(real(Extension),3),' [%]'])
end
figure2     = figure('units','normalized','position',[0.54375 0.506836 0.4375 0.410156]);
Extension   = ((X(:,end)-X(:,1))-width)/width*100;
plot(Extension,H(:,round(nx/2)),'-k',Extension,H(:,1),'--k'); hold on
Extension   = ((Xcs(:,end)-Xcs(:,1))-width)/width*100;
plot(Extension,Hcs(1:end-1,round(nx/2)),'-b',Extension,Hcs(1:end-1,1),'--b')
xlabel('Extension [%]'); ylabel('Thickness [no dimension]'); title(['n = ',num2str(n)])
legend('Neck - constant force','Swell - constant force','Neck - constant rate','Swell - constant rate',3)
```

Appendix C. The finite element algorithm

This appendix summarizes the self-developed finite element algorithm which was used in this study. A modified version of this finite element algorithm, optimized for calculation speed, was used for the simulations with random perturbations and is described in detail in Dabrowski et al. (in press). The conservation equations for slow flow in the absence of body forces in two dimensions are (e.g. Batchelor, 1967; Bathe, 1996; Haupt, 2002):

$$\frac{\partial \sigma_{xx}}{\partial x} + \frac{\partial \sigma_{xy}}{\partial y} = 0$$
$$\frac{\partial \sigma_{xy}}{\partial x} + \frac{\partial \sigma_{yy}}{\partial y} = 0 \tag{A1}$$

$$\frac{\partial p}{\partial t} = -K\left(\frac{\partial v_x}{\partial x} + \frac{\partial v_y}{\partial y}\right) \tag{A2}$$

where σ_{xx} and σ_{yy} are components of the total stress tensor for the x- and y-direction, respectively, σ_{xy} is the shear stress, p is the pressure, K is the compressibility parameter and v_x and v_y are the velocities in the x- and y-direction. (A1) represents conservation of linear momentum and (A2) represents conservation of mass. Here, incompressible flow only is considered. (A2) deviates from the standard form for incompressible flow, i.e.

$$\frac{\partial v_x}{\partial x} + \frac{\partial v_y}{\partial y} = 0,$$

but is only applied here for very large values of K, so that the resulting divergence of the velocity field goes to zero, which means to 10^{-15} in this study, and the material is effectively incompressible. Application of (A2) is often referred to as the penalty approach for incompressible flow (Cuvelier et al., 1986; Hughes, 1987). The constitutive equations for a power-law rheology are:

$$\begin{Bmatrix} \sigma_{xx} \\ \sigma_{yy} \\ \sigma_{xy} \end{Bmatrix} = -p\begin{Bmatrix} 1 \\ 1 \\ 0 \end{Bmatrix} + \frac{1}{3}\eta_{\text{eff}}\underbrace{\begin{bmatrix} 4 & -2 & 0 \\ -2 & 4 & 0 \\ 0 & 0 & 3 \end{bmatrix}}_{\mathbf{D}}\begin{Bmatrix} \partial v_x/\partial x \\ \partial v_y/\partial y \\ \partial v_x/\partial y + \partial v_y/\partial x \end{Bmatrix} \tag{A3}$$

with η_{eff} being the effective viscosity given by

$$\eta_{\text{eff}} = \eta_0 \varepsilon_{\text{II}}^{\frac{1}{n}-1}, \text{ with } \varepsilon_{\text{II}} = \left[\frac{1}{4}\left(\frac{\partial v_x}{\partial x} - \frac{\partial v_y}{\partial y}\right)^2 + \frac{1}{4}\left(\frac{\partial v_x}{\partial y} + \frac{\partial v_y}{\partial x}\right)^2\right]^{1/2} \tag{A4}$$

and η_0 being the reference viscosity for homogeneous pure shear conditions (i.e. $\varepsilon_{\text{II}} = 1$). Discretization of the governing equations and numerical integration is performed using the isoparametric Q9/3-element with 9 nodes for the biquadratic continuous velocity degrees of freedom and 3 nodes for the linear discontinuous pressure degrees of freedom (Hughes, 1987). After discretization the governing equations are given as (Hughes, 1987):

$$\begin{bmatrix} \mathbf{K} & \mathbf{Q} \\ \mathbf{Q}^T & -\frac{\mathbf{M}}{K\Delta t} \end{bmatrix}\begin{Bmatrix} \tilde{v} \\ \tilde{p}^{\text{new}} \end{Bmatrix} = \begin{Bmatrix} 0 \\ -\frac{\mathbf{M}}{K\Delta t}\tilde{p}^{\text{old}} \end{Bmatrix} \tag{A5}$$

where swung dashes denote vectors containing nodal values of the respective variables. The time derivative in (A2) has been replaced by a finite difference quotient with Δt being the time increment $(\partial p/\partial t \approx (p^{\text{new}} - p^{\text{old}})/\Delta t)$. The three matrices $\mathbf{K}$, $\mathbf{Q}$ and $\mathbf{M}$ are:

$$\mathbf{K} = \int\int\mathbf{B}^T\mathbf{D}\mathbf{B}\mathrm{d}x\mathrm{d}y, \quad \mathbf{Q} = -\int\int\mathbf{B}_G^T\mathbf{N}_P\mathrm{d}x\mathrm{d}y,$$

$$\mathbf{M} = \int\int\mathbf{N}_P^T\mathbf{N}_P\mathrm{d}x\mathrm{d}y \tag{A6}$$

where vector $\mathbf{N}_P$ contains the pressure shape functions and matrix $\mathbf{B}$ and vector $\mathbf{B}_G$ contain spatial derivatives of the velocity shape functions in a suitable organized way (Zienkiewicz and Taylor, 1994). The integrations are performed numerically using 9 integration points per element. Using discontinuous pressure shape functions allows the elimination of the pressure at the element level. This elimination leads to a system involving only unknown velocities:

$$\mathbf{L}\tilde{v} = -\mathbf{Q}\tilde{p}^{\text{old}} \tag{A7}$$

where

$$\mathbf{L} = \mathbf{K} + K\Delta t\mathbf{Q}\mathbf{M}^{-1}\mathbf{Q}^T \tag{A8}$$

Values of $\tilde{p}^{\text{new}}$ are restored during the Uzawa-type iteration algorithm, during which (A7) is solved iteratively with updated values of $\tilde{p}^{\text{old}}$ until the divergence of the velocity converges towards zero (i.e. 10^{-15}, e.g., Pelletier et al., 1989). After every time step, the resulting velocities are used to move the nodes of each element with the displacements resulting from the product of velocities times time step (i.e. explicit time integration). Then, the new velocities are again calculated for the new grid.

The non-linearity of the power-law material is treated with Picard iterations, which exhibit a large radius of convergence. The code is structured so that the Uzawa iteration loop is the innermost, nested inside the power-law loop. Convergence studies reveal that the easily reachable criterion on incompressibility of 10^{-15} (normalized over the background strain rate) is more than sufficient; however, it is crucial that a rather tough Picard iteration criterion is used. In the presented numerical experiments it was required that the absolute value of the velocity differences, stored on the vector Δv, between two Picard iteration steps, p, anywhere in the computational domain fulfils:

$$\left[\max(\Delta v^p) - \max(\Delta v^{p-1})\right]/\max(\Delta v^p) \le 10^{-5} \tag{A9}$$

Since a Lagrangian moving mesh approach is chosen in order to accurately resolve the evolution of the geometry and related parameters re-meshing is employed once the mesh is too strongly deformed.

The developed finite element algorithm has been successfully tested with several analytical solutions. The FEM code correctly reproduced (i) the analytical growth rates (Fletcher, 1977) for single-layer folding, (ii) the analytical growth rates for power-law necking (Fig. 2), and (iii) the analytical pressure field around a rigid inclusion (Schmid and Podladchikov, 2003).

References

Bassi, G., Bonnin, J., 1988. Rheological modeling and deformation instability of lithosphere under extension. Geophysical Journal-Oxford 93 (3), 485–504.

Batchelor, G.K., 1967. An Introduction to Fluid Dynamics. Cambridge University Press, Cambridge.

Bathe, K.-J., 1996. Finite Element Procedures. Prentice Hall, Upper Saddle River, New Jersey.

Biot, M.A., 1961. Theory of folding of stratified viscoelastic media and its implications in tectonics and orogenesis. Geological Society of America Bulletin 72 (11), 1595−1620.

Braun, J., Beaumont, C., 1989. A physical explanation of the relation between flank uplifts and the breakup unconformity at rifted continental margins. Geology 17 (8), 760−764.

Carter, N.L., Tsenn, M.C., 1987. Flow properties of continental lithosphere. Tectonophysics 136, 27−63.

Cuvelier, C., Segal, A., van Steenhoven, A.A., 1986. Finite element methods and the Navier-Stokes equations. D. Reidel Publishing Company.

Dabrowski, M., Krotkiewski, M., Schmid, D.W. MILAMIN: MATLAB-based FEM solver for large problems. Geochemistry, Geophysics and Geosystems, in press. doi:10.1029/2007GC001719.

Dombard, A.J., McKinnon, W.B., 2001. Formation of grooved terrain on Ganymede: Extensional instability mediated by cold, superplastic creep. Icarus 154 (2), 321−336.

Emerman, S.H., Turcotte, D.L., 1984. A back-of-the-envelope approach to boudinage mechanics. Tectonophysics 110 (3−4), 333−338.

Fletcher, R.C., 1974. Wavelength selection in the folding of a single layer with power-law rheology. American Journal of Science 274 (11), 1029−1043.

Fletcher, R.C., 1977. Folding of a single viscous layer: exact infinitesimal-amplitude solution. Tectonophysics 39, 593−606.

Fletcher, R.C., Hallet, B., 1983. Unstable extension of the lithosphere—a mechanical model for basin-and-range structure. Journal of Geophysical Research 88 (NB9), 7457−7466.

Fletcher, R.C., Sherwin, J.A., 1978. Arc lengths of single layer folds—discussion of comparison between theory and observation. American Journal of Science 278 (8), 1085−1098.

Hart, E.W., 1967. Theory of tensile test. Acta Metallurgica 15 (2), 351−355.

Haupt, P., 2002. Continuum Mechanics and Theory of Materials. Springer, Berlin.

Hudleston, P.J., Holst, T.B., 1984. Strain analysis and fold shape in a limestone layer and implications for layer rheology. Tectonophysics 106 (3−4), 321−347.

Hughes, T., 1987. The Finite Element Method. Dover Publications, Mineola, New York.

Johnson, A.M., Fletcher, R.C., 1994. Folding of Viscous Layers. Columbia University Press, New York.

Kidan, T.W., Cosgrove, J.W., 1996. The deformation of multilayers by layer-normal compression; An experimental investigation. Journal of Structural Geology 18 (4), 461−474.

Kneale, W., Kneale, M., 1985. The Development of Logic. Oxford University Press, Oxford.

Kooi, H., Cloetingh, S., Burrus, J., 1992. Lithospheric necking and regional isostasy at extensional basins, 1, Subsidence and gravity modelling with an application to the Gulf of Lions Margin (SE France). Journal of Geophysical Research 97 (B12), 17553−17572.

Mandal, N., Khan, D., Deb, S.K., 1992. An experimental approach to wide-necked pinch-and-swell structures. Journal of Structural Geology 14 (4), 395−403.

Martinod, J., Davy, P., 1992. Periodic instabilities during compression or extension of the lithosphere.1. Deformation modes from an analytical perturbation method. Journal of Geophysical Research-Solid Earth 97 (B2), 1999−2014.

Nanjo, K.Z., Turcotte, D.L., Shcherbakov, R., 2005. A model of damage mechanics for the deformation of the continental crust. Journal of Geophysical Research-Solid Earth 110 (B7), doi:10.1029/2004JB003438.

Neurath, C., Smith, R.B., 1982. The effect of material properties on growth rates of folding and boudinage: experiments with wax models. Journal of Structural Geology 4, 215−229.

Pelletier, D., Fortin, A., Camarero, R., 1989. Are FEM solutions of incompressible flows really incompressible? (or how simple flows can cause headaches!). International Journal for Numerical Methods in Fluids 9, 99−112.

Pollard, D.D., Fletcher, R.C., 2005. Fundamentals of Structural Geology. Cambridge University Press, Cambridge.

Poplavskii, K.N., Podladchikov, Y.Y., Stephenson, R.A., 2001. Two-dimensional inverse modeling of sedimentary basin subsidence. Journal of Geophysical Research-Solid Earth 106 (B4), 6657−6671.

Price, N.J., Cosgrove, J.W., 1990. Analysis of Geological Structures. Cambridge University Press, Cambridge.

Ramberg, H., 1955. Natural and experimental boudinage and pinch-and-swell structures. Journal of Geology 63 (6), 512−526.

Rüpke, L.H., Schmalholz, S.M., Schmid, D.W., Podladchikov, Y.Y. Automated thermo-tectono-stratigraphic basin reconstruction: Viking Graben case study. American Association of Petroleum Geologists Bulletin, 92 (3), in press. doi:10.1306/11140707009.

Schmalholz, S.M., 2006. Finite amplitude folding of single layers: elastica, bifurcation and structural softening. Philosophical Magazine 86 (21−22), 3393−3407.

Schmalholz, S.M., Podladchikov, Y.Y., 2000. Finite amplitude folding: transition from exponential to layer length controlled growth. Earth and Planetary Science Letters 181 (4), 617−633.

Schmid, D.W., Podladchikov, Y.Y., 2003. Analytical solutions for deformable elliptical inclusions in general shear. Geophysical Journal International 155, 269−288.

Schmid, D.W., Podladchikov, Y.Y., Marques, F.O., 2004. Folding of a finite length power law layer. Journal of Geophysical Research-Solid Earth 109 (B3), doi:10.1029/2003JB002421.

Sherwin, J.A., Chapple, W.M., 1968. Wavelengths of single layer folds—a comparison between theory and observation. American Journal of Science 266 (3), 167−179.

Smith, R.B., 1977. Formation of folds, boudinage, and mullions in non-Newtonian materials. Geological Society of America Bulletin 88 (2), 312−320.

Turcotte, D.L., Glasscoe, M.T., 2004. A damage model for the continuum rheology of the upper continental crust. Tectonophysics 383 (1-2), 71−80.

Zienkiewicz, O.C., Taylor, R.L., 1994. The Finite Element Method. McGraw-Hill Book Company, London.

Zuber, M.T., Parmentier, E.M., 1986. Lithospheric necking—a dynamic-model for rift morphology. Earth and Planetary Science Letters 77 (3-4), 373−383.